High-Voltage, High-Frequency Pulse Generator for Non-Equilibrium Plasma Generation & Combustion Enhancement (April 2016)

Mathew D.G. Evans, Jeffrey M. Bergthorson, and Sylvain Coulombe

***Abstract*— This article outlines the design and implementation of a solid-state high-voltage, high-frequency pulse generator used to drive capacitive loads and particularly, non-equilibrium plasmas at atmospheric pressure. The generator is capable of producing open circuit pulses of 0-12 kV with a 300 ns duration (FWHM) at a repetition frequency of 0-25 kHz. The working principles of the generator are presented, along with its electrical diagnostics to illustrate its operation with capacitive loads. The generator was applied to a pin-to-plane electrode configuration to generate a diffuse non-equilibrium plasma discharge with peak voltage of 12 kV. Energy deposition, and average power required to drive the discharges in open air at 25 kHz were calculated to be 112 µJ/pulse and 2.80 W. The generator was also applied to lean, stagnation-plate stabilized V-shaped flames to increase their blowoff velocity. A 28-51 % increase of the blowoff velocity is observed using a discharge with peak voltage of 6.2 kV, and repetition rate of 25 kHz.**

***Index Terms*— Plasma generation, Plasma devices, Pulse power systems, Atmospheric pressure plasmas**

I. Introduction

In recent years, non-equilibrium plasmas have been increasingly studied in the fields of pollution mitigation [1], under-water discharge generation [2], plasma-assisted combustion [3], ignition [4] and plasma medicine [5], to name a few. Traditionally, AC generators operating in the mid-kHz range are used to generate atmospheric pressure non-equilibrium plasma discharges. These generators constantly deposit energy to the plasma load, leading to a relatively high degree of thermalization of the plasma gas. Atmospheric pressure AC discharges also produce an unpredictable number of unevenly timed current pulses over a single period of the discharge [6]. This makes energy deposition calculations a more complicated task, as additional passive circuit elements must often be added [7]. To mitigate the thermalization problem, the use of repetitive high-voltage and short duration (100-1000 ns) discharges has become increasingly popular as they provide an increased level of non-equilibrium [8][9]. The higher overvoltage conditions also drive the electron-based plasma chemistry producing highly reactive species [10]. Short duration, high-voltage pulses give rise to precise and timed energy deposition to the plasma load.

Activating a gaseous mixture for ignition and combustion applications requires high-voltage pulses to be delivered to the plasma load, at a repetition rate of several kHz. This requirement stems from the need to retain a reasonably high background electron number density in the inter-electrode zone prior to the application of the next voltage pulse to the load [11]. Additionally, flames have lower neutral number densities, and higher ion number densities, which increase the probability of occurrence of spurious spark discharges. Therefore, short-circuit protected, solid-state generators are required to provide high-voltage pulses at high pulse repetition frequencies. Commercially available solid-state generators can be quite costly, and may require frequent maintenance when driving spark-type discharges for extended periods of time. Some studies have focused on designing and developing high-voltage pulse generators for non-equilibrium plasma production at atmospheric pressure [12][13][14]. These require the use of high-voltage solid state switches, or thyristors, which have limited pulse repetition frequencies due to increased power dissipation considerations, and high charging voltage [15][16]. Recently, robust pulsed-power generators have been developed for plasma-assisted ignition applications [17], and some with a maximum burst pulse repetition frequency up to 10 kHz [18].

The objective of this work is to develop a simple, low cost, high-voltage pulse generator to produce diffuse plasmas and, in particular, to apply it to assist the combustion of V-shaped flames. The generator is designed to drive capacitive loads of tens of picofarads, which are typical for laboratory-scale transient non-equilibrium plasma discharge systems [19][20][21]. The generator's architecture and the choice of its circuit components are presented first. Its operability is demonstrated with several capacitive loads, including a pin-to-plate configuration to produce large volume non-equilibrium

This paper was submitted for review on April 17, 2016. This work was supported in part by the Natural Sciences and Engineering Research Council of Canada and Siemens ADGT.

Mathew D. G. Evans is a PhD candidate in the Department of Chemical Engineering, McGill University, Montréal, QC H3A 0C5, Canada (e-mail: mathew.evans@mail.mcgill.ca).

Jeffrey M. Bergthorson is an Associate Professor with the Department of Mechanical Engineering, McGill University, Montréal, QC H3A 0C3, Canada (e-mail: jeffrey.bergthorson@mcgill.ca).

Sylvain Coulombe is a Professor with the Department of Chemical Engineering, McGill University, Montréal, QC H3A 0C5, Canada (e-mail: sylvain.coulombe@mcgill.ca).

plasma discharges in open air. Energy deposition calculations are presented to assess the power consumed by the discharge. Finally, the generator is applied to the combustion of lean premixed methane/air flames to increase their blowoff velocity and sustain combustion in otherwise unstable burning conditions.

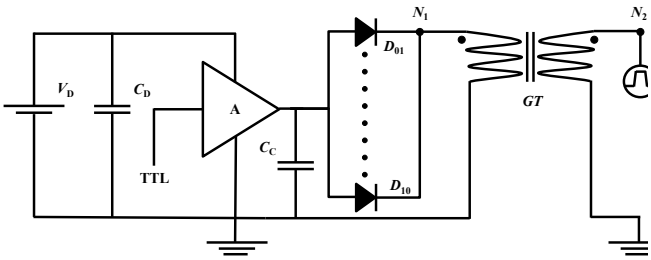

Fig. 1 Equivalent driver circuit of the pulse generator.

II. Pulsed Power Generator

A. Driver Circuit & Short Circuit Protection

Fig. 1 shows the solid-state generator's timing and driver circuit that controls and protects the pulse generator from reflected power in the event of high-current spark discharges. The driver circuit is powered by a DC power supply, V_D, set to 17 V. Capacitor C_D has a value of 4.7 µF, and is used to stabilize V_D. Amplifier *A* is a single output MOSFET driver (*MAXIM*, MAXX4420) and its output stabilizing capacitor, *Incorporated*, 1N4007) consist of a low impedance diode bank with 1 kV hold-off voltage, and *GT* is a 1:1 gate drive transformer (*SMT*, PA0184NL) with 1.5 kV of isolation voltage. Circuit nodes N_1 and N_2 identified on Fig. 1 will be referred to in section 3. The principle of operation is as follows: A 5 V TTL pulse (Δt = 1 µs) is supplied by the low voltage pulse generator (*Berkeley Nucleonics*, BNC 575) and is amplified to 18 V by amplifier *A*. The amplified pulse is fed through the diode bank and primary windings of the *GT* before returning to ground. The output from the *GT*'s secondary windings is sent to the primary switching stage of the pulse generator. The purpose of using a stack of parallel diodes in series with a gate drive transformer is to combine their isolation voltage rating to prevent damage to amplifier *A* and the TTL signal generator.

B. Pulse Generator Circuit Architecture

The equivalent circuit of the pulse power generator is presented in Fig. 2. The circuit is resistively charged by an adjustable output DC power supply, V_{DC} (*Sorensen*, XG-600-1.4) through resistor R_{DC} (104 Ω). Diode D_{DC} serves as a protective barrier for the DC power supply. Diode D_S allows the magnetization current to keep flowing through pulse transformer *PT*, while switch *S* is closed. D_{DC} and D_S are both ultrafast diodes (*Fairchild Semiconductor*, RURG80100) with high surge current handling capabilities. Capacitor C_{DC} is a 1 µF filter capacitor used to stabilize the power source, and reduce the jitter in the output pulse. Capacitor C_1 is made up of two polypropylene capacitors placed in parallel with an equivalent capacitance of 69 nF. The solid-state switch, *S*, is comprised of two parallel high-speed insulated gate bipolar transistors (IGBTs) to accommodate the moderate current handling requirements and the relatively high switching frequency for continuous operation. The IGBTs (*IXYS*, IXYH60N90C3) are rated for an operating voltage of 900 V, and a combined maximum current handling capability of 310 A in pulse mode.

Pulse transformer PT is a nanocrystalline core (Hitachi Metals, Ltd., F1AH0898) with a saturation magnetic flux density of 1.23 T and a relative permeability of $15 \cdot 10^3$ at a frequency of 100 kHz. Two and forty-two turns of 18 AWG magnet wire are used as primary and secondary windings, respectively. Capacitor C_2 (405 pF) is a ceramic disc capacitor with a DC voltage rating of 15 kV. The value of capacitor C_2 affects the rise time and amplitude of the voltage waveform applied to the electrodes. In other words, as the value of C_2 increases, so does the voltage pulse amplitude and pulse width that can be applied at the output of the generator. Variable inductor L_1 is a single nanocrystalline core (Hitachi Metals, Ltd., F1AH0896) with 30 turns of AWG20 magnet wire, used as an internal choke and to control the fall time of the output voltage waveform. Resistor R_{stab} (19.2 kΩ) is a ceramic resistor bank (Kanthal Globar), which stabilizes the output of the pulse generator and reduces jitter. The generator can be

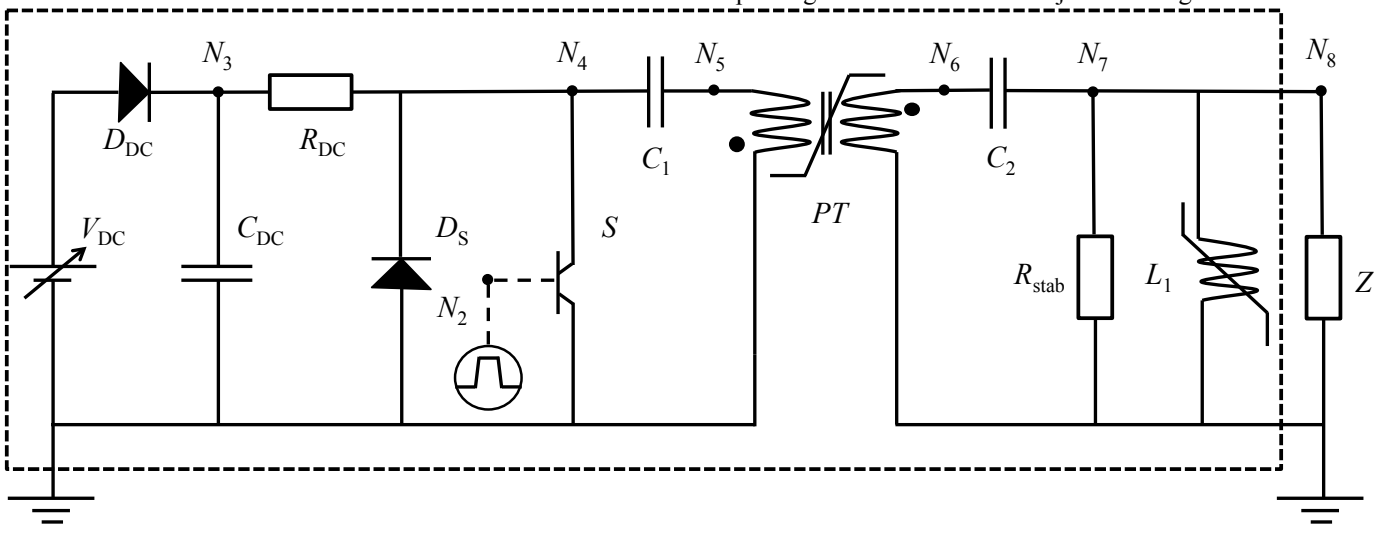

Fig. 2 Equivalent circuit of the pulsed power generator, inside the dashed line, connected to an external load Z.

connected to an external load, *Z,* using a high-voltage coaxial cable (*Essex*, 21-908 RG 8/U) with characteristic impedance of 50 Ω. For this study, ceramic capacitors (section *III*), a pin-to-plane electrode (section *V.A.*), and a combustion apparatus (section *V.B.*) were used as external loads. The total cost of the components of this generator, including an enclosure and cooling fans is under 500 USD.

C. Electrical Diagnostics

Low voltage (0-630 V) measurements were made using a 10X passive voltage probe (*Tektronix,* P6106, 13 pF, 10 MΩ). All high-voltage measurements were made using a 1000X passive probe (*Tektronix,* P6015A, 3 pF, 100 MΩ). The current through the load was measured using a wideband current transformer (*Pearson Electronics*, Model 110A, 10 A/V). The electrical measurements were recorded using a high-speed digital oscilloscope (*Tektronix,* TDS-3054B). Synchronization of all electrical measurements was accomplished using the BNC 575 pulse generator.

III. Operation of the Pulse Generator

Fig. 3 shows the equivalent test circuit and voltages at nodes N_1-N_8 of the driver and pulse generator circuits presented in Figs. 1-2. All tests and diagnostics in this section were performed at a pulse repetition frequency of 10 kHz. Fig. 3 a) shows the connection configuration of the load and coaxial cable in parallel, forming an equivalent capacitance. Fig. 3 b) shows the operation of the driver circuit for the TTL trigger signal, amplified TTL signal at node N_1, and output from GT's secondary windings at node N_2 by the solid, dashed and finely dashed curves, respectively. Fig. 3 c) shows the operation of the low voltage circuit for circuit nodes N_3-N_5, again identified in the same sequence of line styles as Fig 3 b). Fig. 3 d) shows the operation of the high-voltage circuit for nodes N_6-N_8 with the same line scheme as Fig. 3 b).

Capacitors C_1 and C_{DC} are initially charged up to the power supply's voltage, V_{DC}. When the transistor bank S is triggered, C_1 fully discharges through the transistor bank and the primary windings of the pulse transformer, while C_{DC} minimally discharges through resistor R_{DC}, limiting the surge requirement of the power supply. This can be seen by the stability of trace V_{N3} in Fig. 3c), which remains at the voltage set point of the power supply with little decrease during transistor breakdown. The transistor breakdown event is characterized simultaneously by voltage waveforms V_{N4} and V_{N5} of Fig. 3 c). These waveforms drive the current through the primary windings of pulse transformer *PT*, and resonantly transfer the energy stored in C_1 to C_2. Once this transfer is complete, and C_2 is fully charged, *PT* saturates and the voltage step-up process is complete. This can be seen by trace V_{N6}. The voltage drop across C_2 is illustrated by comparing waveforms V_{N6} and V_{N7}. The voltage drop along the output coaxial cable can be seen by examining the difference in voltages of

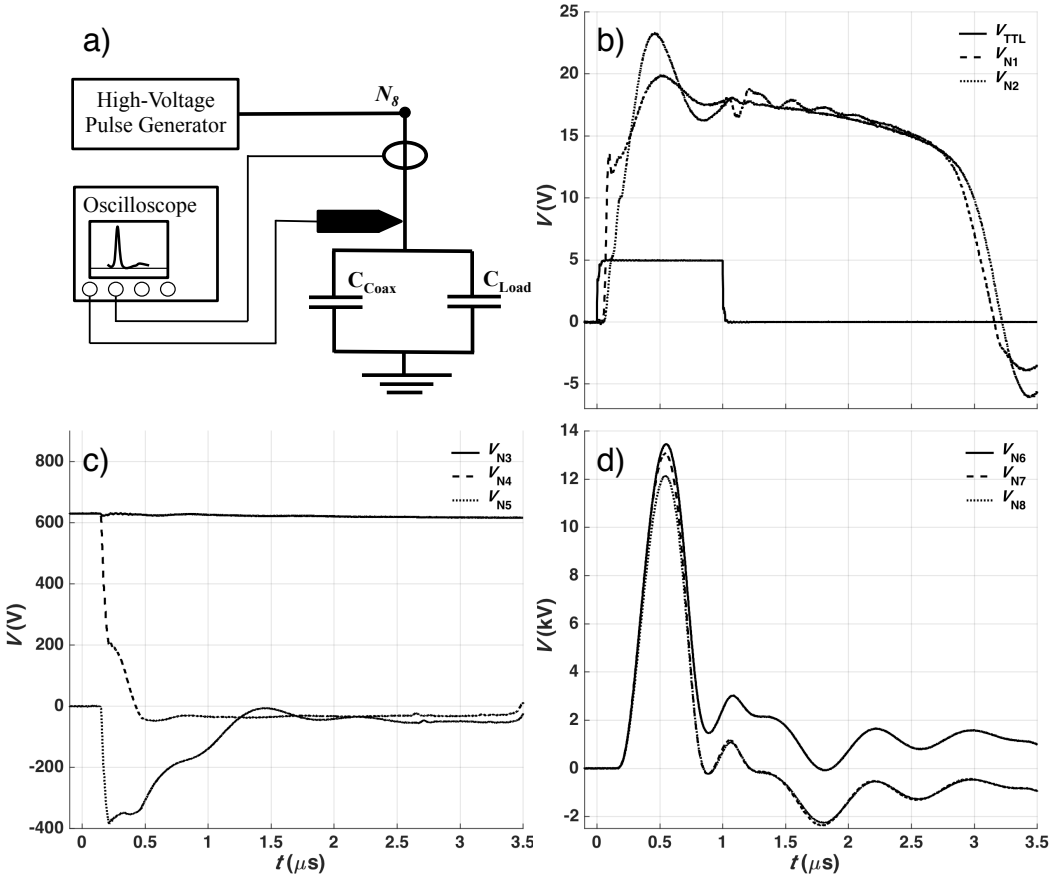

Fig. 3 Test circuit (a) and electrical diagnostics of the: driver circuit (b), the low voltage circuit (c), and high-voltage circuit (d) for C_{load} = 0 pF.

waveforms V_{N7} and V_{N8}.

Fig. 4 shows the peak voltage and current of the generator as a function of the capacitance of the external load (C_{load} = 0-100 pF), and the charging voltage of the source (V_{DC} = 200, 400, 630 V). As the load capacitance increases, the peak voltage decreases and the peak current increases, which is the expected behavior for capacitive loads. The capacitance of the coaxial cable was calculated to be 10 pF by measuring the voltage and current at the output of the coaxial cable with no external load (C_{load} = 0 pF), as was done in Fig. 3. The displacement current was calculated from the output voltage waveform with Eq. 1. The value of the cable capacitance was then adjusted so that the total measured current in the cable was equal to the calculated displacement current.

$$I_{disp} = C_{cable}\left(\frac{dV}{dt}\right) \quad (1)$$

Fig. 5 a) shows the effect of the load capacitance on the output pulse, for a fixed charging voltage of 630 V. Fig. 5 b) shows the effect of the input voltage from the source on the output voltage waveform. As the load capacitance increases, so does the rise time of the voltage signal, and the pulse width, due to the charging time of the load. For a fixed capacitive load of 20 pF, the primary voltage pulse has a fixed pulse width of 300 ns FWHM, with varying parasitic secondary pulses. It should be noted that these secondary pulses, which remain below 2.2 kV, become less predominant as the capacitance of the external load decreases, and as the charging voltage increases. As V_S increases, for a fixed capacitive load, the pulse width is constant, and the peak value of voltage across the load is directly proportional to it.

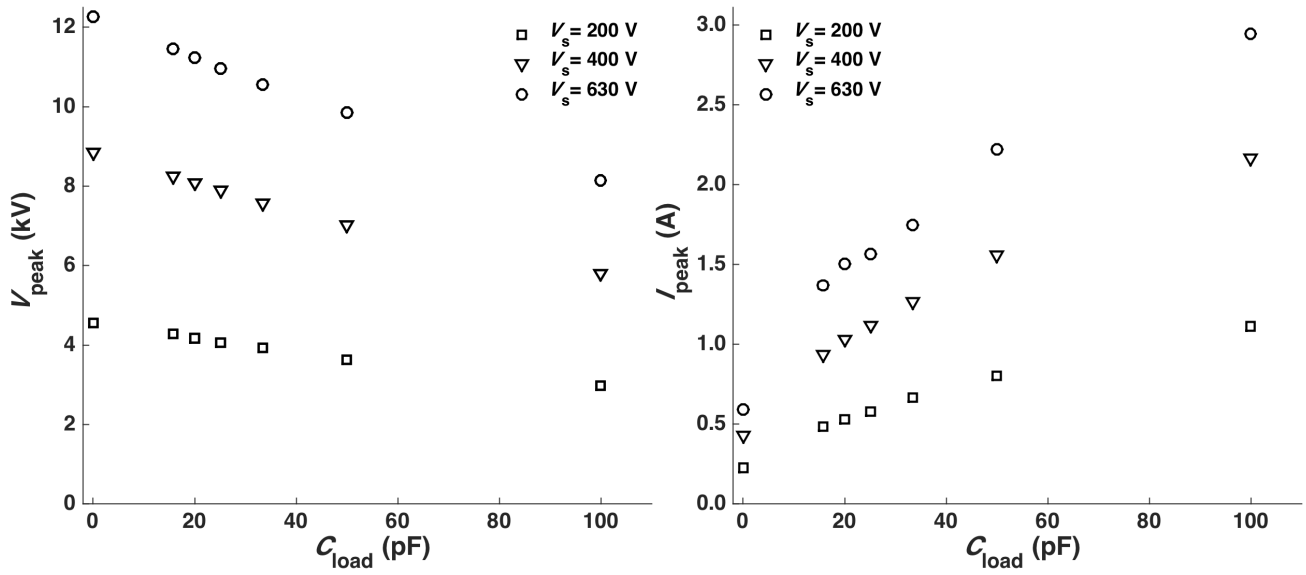

Fig. 4 Peak voltage (left) and peak current (right) as a function of the capacitive load for various DC charging voltages.

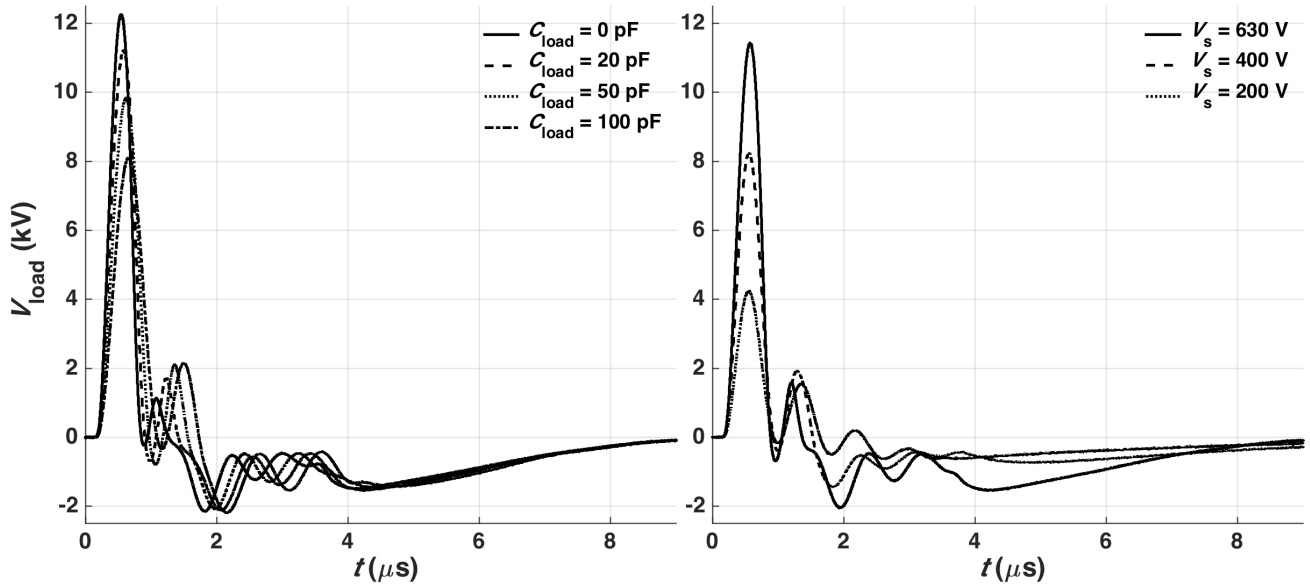

IV. Electrode Configurations, Gas Delivery System, and Stagnation-Plate Burner

Fig. 7 shows the electrode configurations used for non-equilibrium plasma generation (left), and plasma-assisted combustion (right). The two apparatus are essentially identical, except that for non-equilibrium plasma generation, the nozzle was removed to ensure the discharge took place between the pin and the stagnation plate. The pin-to-plane distance, L, was 1.5 cm, and the nozzle inner diameter, D, was 1.6 cm. Cooling water streams CW_{in} and CW_{out}, are the inlet and outlet streams respectively. The nozzle is a stainless steel 304, NW-40-16 conical reducer (*Kurt J. Lesker Company*, QF40XQF16CA) connected to a tee through which the gas supply lines were connected. The high-voltage needle electrode (O.D. = 0.70 mm) and the stagnation plate were both made of stainless steel. In order to avoid undesired arcing to the nozzle and to confine the plasma to the flame environment, the nozzle was coated with a layer of insulating varnish dielectric. The pulse generator is connected to the high-voltage electrode using the previously mentioned coaxial cable, and a high-voltage feedthrough (*MDC Vacuum*, 9443001) with a DC voltage rating of 30 kV. The methane and air gas flow rates were regulated with two mass flow controllers (*Brooks* SLA5850S, 0-20 SLPM and *Brooks* 5851S, 0-50 SLPM, respectively). The stagnation plate was cooled, with a flow of 45 liters per hour of water in order to keep the stagnation plate gaskets intact and free from damage during the experiments.

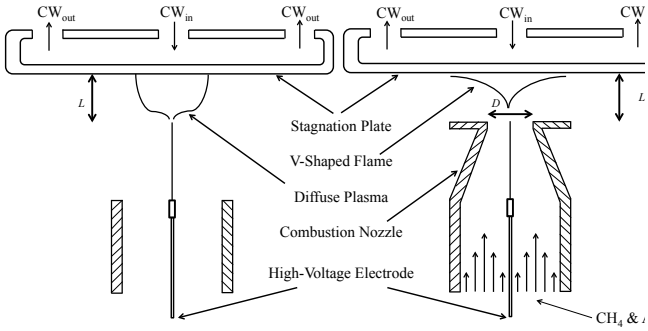

Fig. 6 Schematics of the experimental setups used to produce a pin-to-plate non-equilibrium discharge (left), and the V- shaped flame (right).

V. Application of the Pulse Generator

A. Non-Equilibrium Plasma Generation

Large diffuse plasma volumes are desirable at atmospheric pressure as a continuous source of excited species and high-energy electrons to be used for combustion enhancement. Prior to applying the generator to the combustion enhancement process, non-equilibrium diffuse plasma discharges were generated between the needle electrode and the stagnation plate in open air. High-voltage pulses, with 11.8 kV peak voltage, were applied to the needle electrode using a charging voltage of 600 V. The pulse repetition frequency was increased from 1 to 25 kHz. Fig. 7 shows the change in the discharge appearance as a function of pulse repetition frequency, for a fixed camera exposure time of 5 seconds. At low pulse repetition frequencies, a low intensity glow-like discharge is formed between the needle electrode and the stagnation plate. As the pulse repetition frequency is increased to 25 kHz, so does the intensity and volume of the plasma body, and the inter-electrode gap is fully bridged with a uniform and large non-equilibrium plasma. The increase in brightness is due to the higher number of pulses captured during the camera's exposure times. We also associate this effect to the ease of plasma re-ignition caused by higher average background electron number density through the interruption of electron recombination processes between pulses [11]. In these images, no high-current sparks were detected by the electrical probes or upon visual inspection.

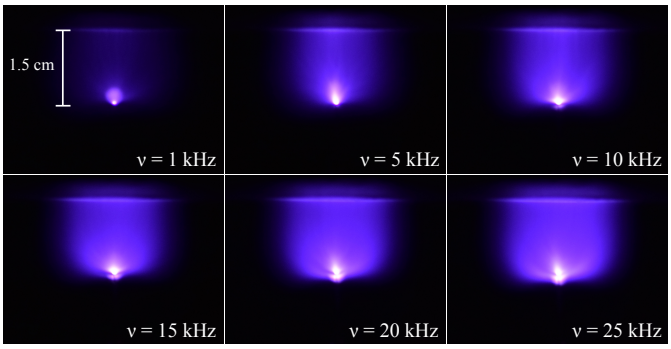

Fig. 7 Images of diffuse non-equilibrium plasma produced in a pin-to-plane configuration spanning the operating range of the pulse generator.

Fig. 8 a) shows the electrical measurements and Fig. 8 b) shows the energy deposited per pulse of the discharge at a pulse repetition frequency of 10 kHz. In Fig. 8 a), the dashed curve represents the total measured current, and the finely dashed curve represents the conduction current through the plasma volume. The displacement current, I_{disp}, was calculated using Eq. 1 for the case of no plasma discharge, and where the capacitance was now $C_{cable+electrodes}$, the combined capacitance of the coaxial cable and electrodes. The vast majority of the measured current is the displacement current. The lumped capacitance of the cable and electrodes was calculated to be 17 pF (7 pF for electrodes and 10 pF for coaxial cable). The conduction current, I_{cond}, was calculated using Eq. 2.

$$I_{cond} = I_{meas} - I_{disp} = I_{meas} - C_{cable+electrodes}\left(\frac{dV}{dt}\right) \quad (2)$$

At a pulse repetition frequency of 10 kHz, the conduction current is a pulse of approximately 250 ns at FWHM, and has a distinct peak value of 72 mA. This waveform is used to calculate the energy deposited per pulse, shown in Fig. 8 b). The energy deposited per pulse of the discharge at 10 kHz is 149 µJ. It should be noted that the negative values of energy deposited are an artifact related to oscillations present in the rise of the displacement current. This behavior was noted for all capacitive loads presented earlier. The value of the

conduction current is lower than a typical DC glow discharge at atmospheric pressure [22].

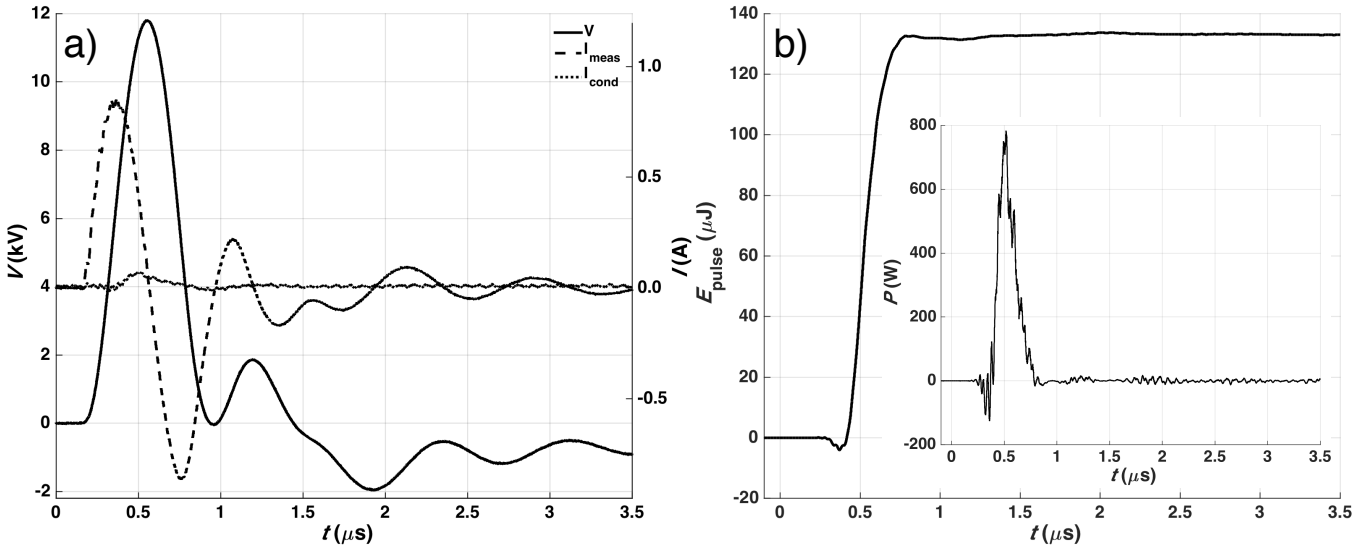

Fig. 8 Applied voltage and current measured at the plasma load (a), energy deposited per pulse of the discharge and instantaneous power (b) for a repetition frequency of 10 kHz.

Fig. 9 shows the energy deposited per pulse, and the average power consumed by the discharge load as a function of the pulse repetition frequency. The instantaneous power is shown in the inset of Fig. 8 b), with a peak value of 776 W. The energy deposited per pulse varies as a function of the pulse repetition frequency. This may be due to the change in frequency-dependent parameters of the magnetic cores, such as permeability and impedance. Nevertheless, the average power consumed by the plasma source in atmospheric pressure air is more heavily influenced by the pulse repetition frequency, which displays a quasi-linear behavior. The maximum average power is 3.2 W at 25 kHz. Since the average power consumption of such a large and uniform plasma body is low, the generator would be ideal to increase the blowoff velocity of our laboratory scale methane-air flames, which have thermal powers in the low kW range, through chemical activation.

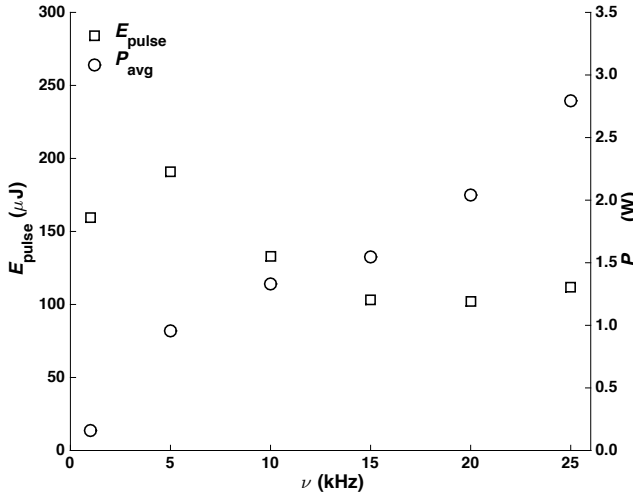

Fig. 9 Energy per pulse coupled to the discharge (a), and average power deposited consumed by the discharge (b) as a function of the pulse repetition frequency.

B. *Flame Stabilization and Anchoring*

Plasma-assisted combustion is being investigated to increase combustion chemical-reaction rates [23][24]. In gas-turbine engines for power generation, increasingly stringent pollutant emissions regulations are driving manufacturers to develop ultra-low-emissions combustion systems. A promising approach is to employ lean-burning combustors to eliminate soot emissions and reduce NO_x, CO, and unburned hydrocarbon pollutant emissions [25]. Lean-burning flames have lower combustion temperatures, which reduce the combustion reaction rates and the speed of propagation of the flame. This can lead to problems in sustaining the flames at high power levels, which correspond to the highest mass flow rates and velocities through the engine. For a given engine flow speed, a lean blowoff limit, or fuel-air concentration, will be found below which the flame extinguishes, the engine loses power, and the unburned fuel can escape through the exhaust [26]. During transient engine operation, such as a rapid power-level shift, the flow conditions and fuel-air mixture composition can be rapidly altered, which can also result in blowoff. As a result, technologies are needed that can increase the reactivity of lean flames in order to improve flame stability.

In this section, we briefly demonstrate that applying the developed plasma generator to V-shaped stagnation plate-stabilized flames (geometry presented in Fig. 6-right) enables the lean blowoff limit to be extended. A more thorough and detailed analysis will be presented in a separate article. The V-shaped flames presented in this article have a qualitatively similar structure to the bluff-body or swirl-stabilized flames found in gas turbine engines and, therefore, capture some of their physical behavior. Prior to discussing flame stabilization

using plasma, some basic combustion quantities are introduced as well as a brief summary of the V-shaped flame's dynamics.

The equivalence ratio, ϕ, of a methane-air flame can be defined by Eq. 3.

$$\phi = \frac{\left(n_{CH_4} / n_{air}\right)}{\left(n_{CH_4} / n_{air}\right)_{st}} \tag{3}$$

where, n_{CH_4} and n_{air} are the molar flow rates of methane and air respectively, and $\left(n_{CH_4} / n_{air}\right)_{st}$ is the stoichiometric methane-to-air ratio needed for complete combustion, having a value of 1/9.52. The speed of the laminar flame propagating into the unburned mixture, s_u, can be estimated using Eq. 4.

$$s_u \cong \frac{\dot{m}}{\rho_u A_{flame}} \tag{4}$$

where $\dot{m}$ is the mass flow rate of gas, ρ_u is the mass density of the unburned mixture, and A_{flame} is the total surface area of the flame. The average velocity of the combustible mixture at the nozzle exit, v_{avg}, can be defined by Eq. 5.

$$v_{avg} = \frac{\dot{m}}{\rho_u A_{nozzle}} \tag{5}$$

where A_{nozzle} is the cross sectional area of the combustion nozzle's outlet. The position of the V-shaped flame front is determined by the dynamic balance between the flow field outside of the nozzle, which is related to v_{avg} and s_u. The flame front is located in this flow field, where the local mixture velocity and that of the flame are of equal magnitude. As the bulk velocity of the combustible mixture is varied, this dynamic balance is readjusted and the position of the flame front changes. If v_{avg} is increased, for a mixture of given ϕ, the flame front will be displaced further downstream from the nozzle's outlet. When a high enough v_{avg} has been imposed, the balance between v_{avg} and s_u cannot be maintained, and the flame blows off at the blowoff velocity, v_b. To mitigate blowoff, s_u must be increased through chemical or thermal activation by the addition of reactive species or heat.

The pulse generator is used as a source of reactive molecules to chemically activate the flame with minimal thermal contributions. Fig. 10 shows the application of the pulse generator to a V-shaped, stagnation plate-stabilized, flame. The left and middle sections of Fig. 10 show that, without plasma actuation, the flame front's base is lifted from the nozzle's outlet. Once plasma actuation is applied, the flame front's base is lowered to the high-voltage electrode tip. The middle and right sections of Fig. 10 show this shift through the use of the white dashed lines comparing the location of the flame front's base. Also Fig. 10 shows that no change in the flame's surface takes place following plasma activation, and that the plasma runs through the flame's entire surface, bridging the inter electrode gap, without the formation of a spark channel. This further classifies the plasma as a glow-like non-equilibrium discharge [27] [28]. Due to the length of the camera's exposure time, thousands of discharge events are captured, and can be seen in the right section of Fig. 10.

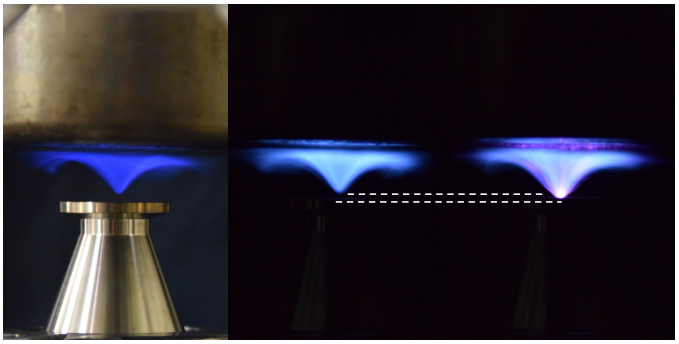

Fig. 10 Stabilization and anchoring of a lean premixed flame (v = 1.5 m/s, ϕ = 0.7, P = 673 W) showing the outline of the flame with the laboratory lights on (left), lights off without plasma activation (middle), and lights off with plasma actuation [ν = 20 kHz, V_{peak} = 6.2 kV] (right).

Fig. 11 shows the uniformity of the applied voltage pulses for pulse repetition frequencies ranging from 1 to 25 kHz, and the increase of the blowoff velocity for equivalence ratios of 0.65 to 0.75. No significant difference in pulse amplitude or pulse width was observed for both the first and second pulse presented in the left part of Fig. 11. We believe that the observed difference in the voltage traces after 1.5 µs is related to the magnetic cores, as was discussed in section 5.1. These differences are not likely to cause additional ionization or energy deposition in the inter-electrode gap as the small conduction current has already decayed at this point in time, as was seen in section 5.1.

It should be mentioned that the voltage pulse amplitude was carefully selected to avoid the formation of spark discharges, which are most likely to occur at the generator's highest pulse repetition frequency, for the lowest bulk mixture velocity and for the hottest flame temperature. First, the generator's pulse repetition frequency was set to 25 kHz, the bulk mixture velocity was set to a low value (v_{avg} = 1.5 m/s) for the most fuel-rich flame (ϕ = 0.75). Then, the voltage amplitude was increased to the maximum allowable value for a glow-like discharge to be formed. The blowoff velocity is found for a fixed equivalence ratio by setting the methane-air mixture velocity to 1.5 m/s, applying the discharge waveform to the electrode, and increasing v_{avg} in increments of 0.05 m/s. It should be mentioned that the initial power of the flames (v_{avg} = 1.5 m/s) for ϕ = 0.65, 0.70, and 0.75 were 628 W, 673 W and 718 W, respectively.

As v_{avg} increased, the flame's attachment to the electrode was monitored until v_b was reached, and the flame was blown off. For each equivalence ratio, the pulse repetition frequency was varied between 1 and 25 kHz, and v_b was recorded. The

blowoff velocity of the flames increased for the equivalence ratios explored. The thermal power of the flames at blowoff and 25 kHz for ϕ = 0.65, 0.70 and 0.75 were 0.96 kW, 1.30 kW and 1.77 kW, respectively. The increases in the blowoff velocity, and power at blowoff, were 28 %, 35 % and 51 % for equivalence ratios ϕ = 0.65, 0.70 and 0.75, respectively. As mentioned earlier, no significant change in of ϕ, while m was continually increased. Therefore the value of s_u necessarily increased through plasma activation.

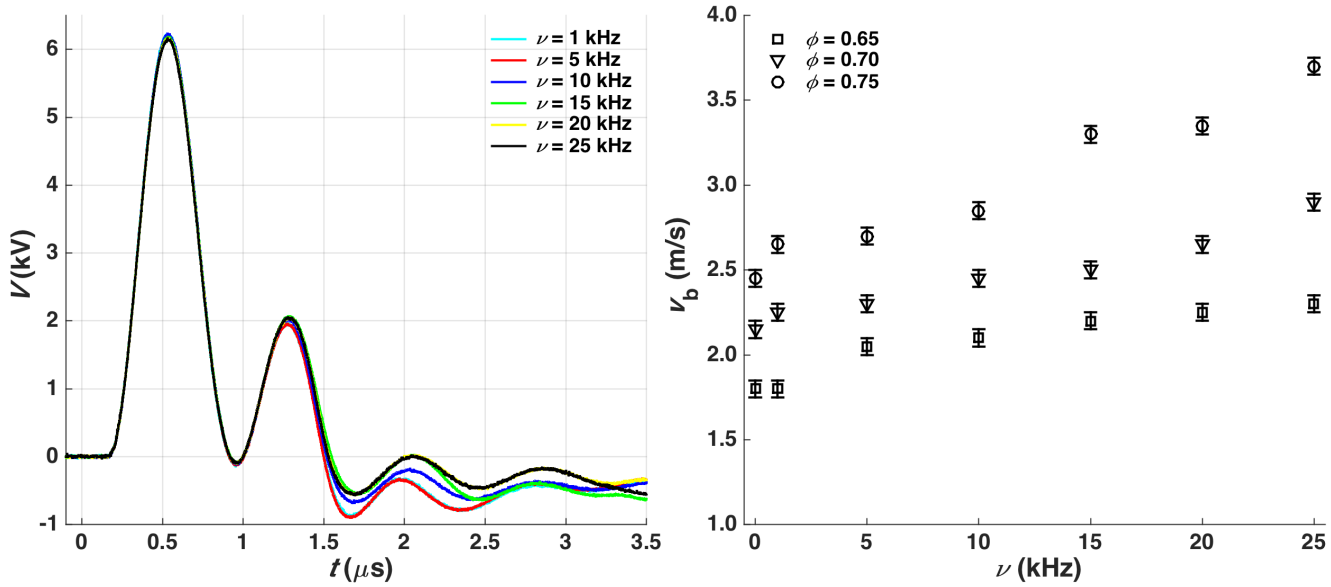

Fig. 11 Applied voltage pulse to the flame for all the pulse repetition frequencies (left), and blowoff velocity as a function of the plasma pulse frequency (right).

VI. Conclusion

A simple and inexpensive (~500 USD) high-voltage/high-repetition rate pulse generator was designed for driving capacitive loads and is capable of sustaining glow-like discharges at atmospheric pressure. The generator characteristics were explored by connecting various capacitive loads and monitoring the peak voltage and current. In a pin-to-plane configuration in open air at 10 kHz, the energy deposition per pulse was 149 μJ, and the peak instantaneous power was 776 W. The total average power consumption was below 3 W at 25 kHz of pulse repetition frequency. The generator was used for the plasma activation of methane-air V-shaped combustion flames. Increases of the blowoff velocity of 28 %, 35 % and 51 % were observed for flames of lean stoichiometry (ϕ = 0.65, 0.70, 0.75).

VII. Acknowledgement

Mathew D.G. Evans would like to acknowledge the financial support provided by the MEDA Tomlinson Doctoral Award, and the FRQNT B2 doctoral award. The authors would like to acknowledge the technical advice provided by electronics specialists Lou Cusmich and Gerald Lepkyj of McGill University and Prof. F.P. Sainct. The authors acknowledge the financial support from the Natural Sciences and Engineering Research Council of Canada and the Fonds de recherche Nature et technologies du Québec.

References

[1] T. Matsumoto, D. Wang, T. Namihira, and H. Akiyama, "Energy efficiency improvement of nitric oxide treatment using nanosecond pulsed discharge," *IEEE Trans. Plasma Sci.*, vol. 38, no. 10, pp. 2639–2643, 2010.

[2] M. Akiyama, Z. Yang, S. Gnapowski, S. H. R. Hosseini, and H. Akiyama, "Observation of Underwater Streamer Discharges Produced by Pulsed Power Using High-Speed Camera," *IEEE Trans. Plasma Sci.*, vol. 42, no. 10, pp. 3215–3220, Oct. 2014.

[3] Y. Ju and W. Sun, "Plasma assisted combustion: Dynamics and chemistry," *Prog. Energy Combust. Sci.*, vol. 48, pp. 21–83, 2015.

[4] Z. Yin, K. Takashima, and I. V Adamovich, "Ignition time measurements in repetitive nanosecond pulse hydrogen-air plasmas at elevated initial temperatures," *IEEE Trans. Plasma Sci.*, vol. 39, no. 12, pp. 3269–3282, 2011.

[5] D. Dobrynin, G. Fridman, G. Friedman, and A. Fridman, "Physical and biological mechanisms of direct plasma interaction with living tissue," *New J. Phys.*, vol. 11, 2009.

[6] S. Zhang, W. Wang, P.-C. Jiang, and D.-Z. Yang, "Comparison of atmospheric air plasmas excited by high-voltage nanosecond pulsed discharge and sinusoidal alternating current discharge," *J. Appl. Phys.*, vol. 114, 2013.

[7] M. Haibao, Y. Lin, L. Ping, T. Chenglong, W. Jinhua, and Z. Guanjun, "Study on the Enhancement Effect of Dielectric Barrier Discharge on the Premixed Methane/Oxygen/Helium Flame Velocity," *Plasma Sci. Technol.*, vol. 17, no. 12, pp. 1019–1026, 2015.

[8] M. D. G. Evans, F. P. Sainct, F. Aristizabal, J. M. Bergthorson, and S. Coulombe, "Development of a nanosecond pulsed HV atmospheric pressure plasma source: preliminary assessment of its electrical characteristics and degree of thermal nonequilibrium," *J. Phys. D. Appl. Phys.*, vol. 48, no. 25, p. 255203, 2015.

[9] W. Kim, H. Do, M. G. Mungal, and M. A. Cappelli, "Flame Stabilization Enhancement and NOx Production using Ultra Short Repetitively Pulsed Plasma Discharges," *44th Aerosp. Sci. Meet. Exhib.*, no. January, pp. 1–13, 2006.

[10] S. V Pancheshny, S. V Sobakin, S. M. Starikovskaya, and A. Y. Starikovskii, "Discharge Dynamics and the Production of Active Particles in a Cathode-Directed Streamer," vol. 26, no. 12, pp.

1054–1065, 2000.

[11] C. H. Kruger, C. O. Laux, L. Yu, D. M. Packan, and L. Pierrot, "Nonequilibrium discharges in air and nitrogen plasmas at atmospheric pressure," *Pure Appl. Chem.*, vol. 74, no. 3, pp. 337–347, 2002.

[12] A. J. M. Pemen, I. V Grekhov, E. J. M. van Heesch, K. Yan, S. A. Nair, and S. V Korotkov, "Pulsed corona generation using a diode-based pulsed power generator," *Rev. Sci. Instrum.*, vol. 74, no. 10, p. [13] A. Pokryvailo, M. Wolf, Y. Yankelevich, E. Abramzon, and Treatment of Pollutants in Heterogeneous Media," *IEEE Trans. Plasma Sci.*, pp. 1188–1191, 2005.

[14] L. Li, Y.-L. Liu, Y.-F. Ge, Y. Bin, J.-J. Huang, and F.-C. Lin, "Generating diffuse discharge via repetitive nanosecond pulses and line-line electrodes in atmospheric air," *Rev. Sci. Instrum.*, vol. 84, [15] Y. Yankelevich, M. Wolf, R. Baksht, A. Pokryvailo, J. Vinogradov, corona discharge: the pulse repetition rate effect," *Plasma Sources Sci. Technol.*, vol. 16, no. 2, pp. 386–391, May 2007.

[16] A. Pokryvailo, Y. Yankelevich, M. Wolf, E. Abramzon, S. Wald, and A. Welleman, "A high-power pulsed corona source for pollution control applications," *IEEE Trans. Plasma Sci.*, vol. 32, no. 5, pp. 2045–2054, 2004.

[17] D. R. Singleton, A. Kuthi, J. M. Sanders, M. A. Gundersen, A. Simone, and S. J. Pendleton, "Low energy compact power modulators for transient plasma ignition," *IEEE Trans. Dielectr. Electr. Insul.*, vol. 18, no. 4, pp. 1084–1090, 2011.

[18] S. J. Pendleton, D. Singleton, A. Kuthi, and M. A. Gundersen, "Compact solid state high repetition rate variable amplitude pulse generator," *2009 IEEE Pulsed Power Conf.*, pp. 922–925, 2009.

[19] D. L. Rusterholtz, D. A. Lacoste, G. D. Stancu, D. Z. Pai, and C. O. Laux, "Ultrafast heating and oxygen dissociation in atmospheric pressure air by nanosecond repetitively pulsed discharges," *J. Phys. D. Appl. Phys.*, vol. 46, no. 46, p. 464010, Nov. 2013.

[20] B. Dou, J. Li, W. Liang, T. Zhu, Y. Li, Y. Jin, and L. He, "Volatile Organic Compounds (VOCs) Removal by Using Dielectric Barrier Discharge," in *2008 2nd International Conference on Bioinformatics and Biomedical Engineering*, 2008, pp. 3945–3948.

[21] A. Flores-Fuentes, R. Pena-Eguiluz, R. Lopez-Callejas, A. Mercado-Cabrera, R. Valencia-Alvarado, S. Barocio-Delgado, and A. de la Piedad-Beneitez, "Electrical Model of an Atmospheric Pressure Dielectric Barrier Discharge Cell," *IEEE Trans. Plasma Sci.*, vol. 37, no. 1, pp. 128–134, 2009.

[22] A. P. Yalin, C. O. Laux, C. H. Kruger, and R. N. Zare, "Spatial profiles of N2+ concentration in an atmospheric pressure nitrogen glow discharge," *Plasma Sources Sci. Technol.*, vol. 11, no. 3, pp. 248–253, 2002.

[23] S. M. Starikovskaia, "Plasma-assisted ignition and combustion: nanosecond discharges and development of kinetic mechanisms," *J. Phys. D. Appl. Phys.*, vol. 47, no. 35, p. 353001, Sep. 2014.

[24] A. Y. Starikovskii, N. B. Anikin, I. N. Kosarev, E. I. Mintoussov, M. M. Nudnova, A. E. Rakitin, D. V. Roupassov, S. M. Starikovskaia, and V. P. Zhukov, "Nanosecond-Pulsed Discharges for Plasma-Assisted Combustion and Aerodynamics," *J. Propuls. Power*, vol. 24, no. 6, pp. 1182–1197, 2008.

[25] J. M. Bergthorson and M. J. Thomson, "A review of the combustion and emissions properties of advanced transportation biofuels and their impact on existing and future engines," *Renew. Sustain. Energy Rev.*, vol. 42, pp. 1393–1417, 2015.

[26] S. J. Shanbhogue, S. Husain, and T. Lieuwen, "Lean blowoff of bluff body stabilized flames: Scaling and dynamics," *Prog. Energy Combust. Sci.*, vol. 35, no. 1, pp. 98–120, 2009.

[27] F. Tholin, D. L. Rusterholtz, D. A. Lacoste, D. Z. Pai, S. Celestin, J. Jarrige, G. D. Stancu, A. Bourdon, and C. O. Laux, "Images of a Nanosecond Repetitively Pulsed Glow Discharge Between Two Point Electrodes in Air at 300 K and at Atmospheric Pressure," *IEEE Trans. Plasma Sci.*, vol. 39, no. 11, pp. 2254–2255, Nov. 2011.

[28] F. P. Sainct, D. A. Lacoste, and C. O. Laux, "Temporal evolution of the glow and spark regimes of nanosecond repetitively pulsed discharges in water vapor," *IEEE Trans. Plasma Sci.*, vol. 42, no. 10, pp. 2620–2621, 2014.